Experimental study of the ^{66}Ni(d, p) ^{67}Ni one-neutron transfer reaction

J. Diriken,[1,2] N. Patronis,[1,3] A. Andreyev,[1,4,5] S. Antalic,[6] V. Bildstein,[7] A. Blazhev,[8] I. G. Darby,[1] H. De Witte,[1] J. Eberth,[8] J. Elseviers,[1] V. N. Fedosseev,[9] F. Flavigny,[1] Ch. Fransen,[8] G. Georgiev,[10] R. Gernhauser,[7] H. Hess,[8] M. Huyse,[1] J. Jolie,[8] Th. Kröll,[7] R. Krücken,[7] R. Lutter,[11] B. A. Marsh,[9] T. Mertzimekis,[12] D. Muecher,[7] R. Orlandi,[1,5,13] A. Pakou,[3] R. Raabe,[1] G. Randisi,[1] P. Reiter,[8] T. Roger,[1] M. Seidlitz,[8] M. Seliverstov,[1,9] C. Sotty,[10] H. Tornqvist,[14] J. Van De Walle,[14] P. Van Duppen,[1] D. Voulot,[9] N. Warr,[8] F. Wenander,[9] and K. Wimmer[7]

[1]*KU Leuven, Instituut voor Kern- en Stralingsfysica, Celestijnenlaan 200D, B-3001 Leuven, Belgium*
[2]*Belgian Nuclear Research Centre SCK·CEN, Boeretang 200, B-2400 Mol, Belgium*
[3]*Department of Physics and HINP, The University of Ioannina, GR-45110 Ioannina, Greece*
[4]*Department of Physics, University of York, YO10 5DD, United Kingdom*
[5]*Advanced Science Research Center, Japan Atomic Energy Agency (JAEA), Tokai-mura, 319-1195, Japan*
[6]*Department of Nuclear Physics and Biophysics, Comenius University, 84248 Bratislava, Slovakia*
[7]*Physik Department E12, Technische Universität München, D-85748 Garching, Germany*
[8]*IKP, University of Cologne, D-50937 Cologne, Germany*
[9]*AB Department, CERN 1211, CH-Geneva 23, Switzerland*
[10]*CSNSM, CNRS/IN2P3, Universite Paris-Sud 11, UMR8609, F-91405 ORSAY-Campus, France*
[11]*Fakultät für Physik, Ludwig-Maximilians-Universität München, D-85748 Garching, Germany*
[12]*INP, NCSR "Demokritos", GR-15310, Ag. Paraskevi/Athens, Greece*
[13]*School of Engineering, University of the West of Scotland, Paisley, PA1 2BE, United Kingdom, and the Scottish Universities Physics Alliance (SUPA)*
[14]*PH Department, CERN 1211, CH-Geneva 23, Switzerland*

(Received 25 February 2015; revised manuscript received 28 April 2015; published 20 May 2015)

The quasi-SU(3) sequence of the positive parity $\nu g_{9/2}$,$d_{5/2}$,$s_{1/2}$ orbitals above the $N = 40$ shell gap are assumed to induce strong quadrupole collectivity in the neutron-rich Fe ($Z = 26$) and Cr ($Z = 24$) isotopes below the nickel region. In this paper the position and strength of these single-particle orbitals are characterized in the neighborhood of ^{68}Ni ($Z = 28$, $N = 40$) through the ^{66}Ni$(d,p)^{67}$Ni one-neutron transfer reaction at 2.95 MeV/nucleon in inverse kinematics, performed at the REX-ISOLDE facility in CERN. A combination of the Miniball γ-array and T-REX particle-detection setup was used and a delayed coincidence technique was employed to investigate the 13.3-μs isomer at 1007 keV in ^{67}Ni. Excited states up to an excitation energy of 5.8 MeV have been populated. Feeding of the $\nu g_{9/2}$ (1007 keV) and $\nu d_{5/2}$ (2207 keV and 3277 keV) positive-parity neutron states and negative parity (νpf) states have been observed at low excitation energy. The extracted relative spectroscopic factors, based on a distorted-wave Born approximation analysis, show that the $\nu d_{5/2}$ single-particle strength is mostly split over these two excited states. The results are also compared to the distribution of the proton single-particle strength in the ^{90}Zr region ($Z = 40, N = 50$).

DOI: 10.1103/PhysRevC.91.054321 PACS number(s): 21.10.−k, 25.45.Hi, 25.70.Hi, 27.50.+e

I. INTRODUCTION

In contrast to the properties of ^{68}Ni [1–4], recent experiments point to a swift onset of collectivity in the region below the neutron-rich nickel isotopes ($Z = 28$) between the $N = 40$ and $N = 50$ shell gaps [5–16]. One of the first observations was the β decay of neutron-rich Mn isotopes, which revealed a sharp decrease of the 2_1^+ energies in ^{64,66,68}Fe ($Z = 26$) [5,6] and later in the neutron-rich Cr isotopes ($Z = 24$) [7]. The discovery of a μs isomer in ^{67}Fe proved to be compatible with enhanced deformation in this nucleus [8]. Recently, $B(E2; 2_1^+ \rightarrow 0_1^+)$ values were measured for neutron-rich Fe and Cr isotopes using lifetime measurements [9–11] and Coulomb excitation [12,13], which confirmed the increase in collectivity when approaching $N = 40$. Other experiments like deep-inelastic scattering [14–16] supported these previous findings.

The main reason for this enhanced collectivity is believed to be a combination of the reduction of a somewhat shallow $N = 40$ shell gap (because of the repulsive $\pi f_{7/2} \nu g_{9/2}$ tensor interaction when protons are removed [17]) and the presence of the $\nu g_{9/2}$-$d_{5/2}$-$s_{1/2}$ orbital sequence directly above this gap, which could strongly enhance quadrupole collectivity [18–20]. The latter is supported by the fact that large-scale shell-model calculations that do not include the $\nu d_{5/2}$ orbital in their valance space fail to reproduce the experimental trends [21]. In contrast, recent calculations encompassing enlarged valence spaces including the $\nu d_{5/2}$ orbital provide better agreement with the experimental data [19,22]. It should be noted that in the calculations of Ref. [19] the quadrupole-quadrupole interaction of the $\nu g_{9/2}$, $d_{5/2}$ orbitals is increased by 20%

to correct for the absence of the $\nu s_{1/2}$ orbital in the valence space. The effect of the quadrupole coherence generated by this quasi-SU(3) sequence ($\Delta j = 2$), containing the $\nu g_{9/2} d_{5/2} (s_{1/2})$ partners, depends on their relative energy separation and thus on the $N = 50$ gap size. Recent calculations have shown that this particular gap size depends, because of three-body monopole forces [23], on the occupancy of the $\nu g_{9/2}$ orbital itself (see Fig. 3 in Ref. [24]). These calculations suggest that the $N = 50$ shell gap is established when the $\nu g_{9/2}$ orbital gets filled with neutrons and thus widens when approaching ^{78}Ni (estimated gap size ≈ 5 MeV), hinting to a robust shell closure for the latter [24]. Near the $N = 40$ nucleus ^{68}Ni the $N = 50$ shell gap is considerably weaker, which can lead to enhanced quadrupole collectivity.

The calculations in Ref. [19] assume that the $N = 50$ shell gap evolves in a similar manner as observed in the Zr isotopes [25] in combination with an estimated $N = 50$ $g_{9/2}$-$s_{1/2}$ gap size of 5 MeV in ^{78}Ni. Experimental input on the size of the $N = 50$ shell gap near ^{68}Ni would provide valuable information for these large-scale shell-model calculations as it can serve as an anchor point for the gap-size evolution [19]. Calculations using three-body forces and information from the Zr chain resulted in an estimated $N = 50$ gap size of 1.5–2 MeV near $N = 40$ [19,24,25].

Among the less exotic nickel isotopes, only for the peculiar case of ^{68}Ni the experimental data leads to unresolved, conflicting pictures. $B(E2)$ measurements revealed a clear local minimum in the $B(E2; 2_1^+ \rightarrow 0_1^+)$ systematics and a maximum in the excitation energy of the 2_1^+ state [1–4]. This common fingerprint of magicity, along with the existence of μs isomers in this region [26], is in conflict with mass measurements, where S_{2n} systematics do not reveal an irregularity at $N = 40$ [27,28]. This apparent anomaly was attributed to the parity change between the pf shell below and gd orbitals above the $N = 40$ harmonic oscillator shell gap, requiring at least two neutrons to be excited to form a 2^+ state. From an extreme single-particle shell-model perspective, ^{67}Ni can be described as a one-neutron hole coupled to ^{68}Ni and hence its excitation spectrum is expected to contain a considerable amount of neutron single-particle strength at low energy, mainly from the empty orbitals and hole states from the filled orbitals.

Spectroscopic information on ^{67}Ni is available from a range of experiments [26,29–35]. Data from β decay provided tentative spin assignments and proposed configurations for the lowest excited states up to and including the $9/2^+$ isomer [29]. Deep inelastic and multinucleon transfer reactions identified the position of higher-lying excited states [30–33] and the spins of the first three states was fixed [31,33]. In the most recent deep-inelastic study in Ref. [33], yrast states up to 5.3 MeV were identified, all built on top of the 1007-keV isomer. The magnetic moment of the ground state was measured and its value of $0.601\mu_N$ differs by only 6% from the expected Schmidt value, hinting towards a very pure $\nu p_{1/2}$ ground-state configuration [34]. Finally, from the measurement of the g factor of the 13.3-μs [26] isomeric $9/2^+$ state at 1007 keV resulted a value smaller by a factor of two than expected for a $1g_{9/2}$ configuration [35]. This reduction was attributed to a 2% admixture of proton 1p-1h $M1$ excitations ($f_{7/2}^{-1} f_{5/2}^{1}$) across the $Z = 28$ gap that would strongly affect the g factor [35]. The study in Ref. [33] has shown that the 313- to 694-keV γ-decay sequence has a stretched-quadrupole character. The 13.3-μs half-life of the delayed 313-keV transition is compatible with an M2 transition, while the 150(4)-ps [36] 694-keV transition is consistent with an E2 character. The combination of all this information firmly fixes the spin sequence for 1007 keV, 694 keV, and the ground state to be $9/2^+$, $5/2^-$, and $1/2^-$ respectively.

One-neutron transfer reactions that populated states in both ^{67,69}Ni are a powerful tool to probe the stability of the $N = 40$ subshell closure, test the single-particle character of excited nuclear states, extract the centers of gravity of the neutron orbitals of interest, and determine the size of shell gaps.

In this paper we present the results of a study of ^{67}Ni produced in a ^{66}Ni(d,p)-reaction (Q value, 3.580 MeV [30,37]), favoring transfer with low ℓ values. The obtained experimental angular distributions are compared with distorted-wave Born approximation (DWBA) calculations, allowing spin and parity assignments and relative spectroscopic factors to be reported.

The main findings of this work have already been published in Ref. [38]. In this paper more details on the experimental conditions and the analysis will be presented. In Sec. II details about the experimental setup and measuring conditions are summarized and the newly developed delayed-coincidence technique is discussed. The analysis of the data is presented in Sec. III leading to the results reported in Sec. IV. In Sec. V the obtained results are compared with systematics in the lighter nickel isotopes and proton single-particle systematics in the $N = 50$ isotones near ^{90}Zr. The results are also compared with shell-model calculations including an enlarged neutron valence space.

II. EXPERIMENTAL SETUP

A. Beam production and manipulation

The radioactive ^{66}Ni beam ($T_{1/2} = 54.6$ h [39]) was produced at the ISOLDE facility in CERN by bombarding a 50-g/cm^2 UC_x target with pulses of 1.4-GeV protons with an intensity of $\sim 6 \times 10^{12}$ protons per pulse (average current of 1μA). The interval between these pulses was always an integer multiple of 1.2 s. The target matrix was heated to a temperature of $\sim 2000^\circ$ C to optimize diffusion and effusion times through the tungsten transfer line towards the ionization cavity. Here the nickel isotopes were selectively ionized in a three-step resonant laser ionization process ($\lambda_1 = 305.1$ nm, $\lambda_2 = 611.1$ nm, $\lambda_3 = 748.2$ nm) using the RILIS laser ion source [40,41]. Because of the temperature of the hot cavity, elements with low ionization potentials (IP) can be surface ionized and cause contaminants, such as gallium ($Z = 31$, IP $= 6.0$ eV), to appear in the beam. The level of contamination was checked by comparing data with the RILIS lasers ON (data containing both nickel and contaminants in the beam) with data in laser OFF mode (only contaminants). From this comparison a beam purity of at least 99% ^{66}Ni was determined.

The positively charged nickel beam was extracted from the ion source by applying a 30-kV electrostatic potential and was subsequently sent through the general purpose separator, resulting in a ^{66}Ni beam which was injected in REX-TRAP [42]. In this Penning trap the beam was accumulated during 30 ms

and cooled by interactions with the buffer gas present (usually Ne or Ar). This bunch of ions was thereafter transferred to REX-EBIS, the electron beam ion source, where the ions were brought to a higher charge state (16^+). This leads to an A/q value of 4.125 that does not allow residual background from REX-EBIS. The time necessary to reach this charge state (28 ms) was optimized for the element of interest. Trapping time in REX-TRAP equals this breeding time to synchronize the system.

The bunch of highly charged isotopes was extracted from REX-EBIS and sent through an A/q separator to select one specific ^{66}Ni charge state without contamination from the residual gas ions [43]. For this experiment, the slow extraction technique from REX-EBIS (i.e., a smooth drop of the trapping potential) was used to maximize the spread of the available ions within the 800-μs bunch window.

Afterwards, the beam was accelerated by the REX accelerator, which consists of a low-energy RFQ (max 300 keV/A), IHS structure (up to 0.8 MeV/nucleon), and a high-energy section (0.8–3.0 MeV/nucleon) containing three seven-gap resonators and one nine-gap resonator [44], before being delivered to the experimental setup. The final energy depends on the A/q of the beam and was 2.95 MeV/nucleon in this case. The global transmission efficiency of REX (including trapping and charge breeding) was of the order of 5%–10%.

A 100-μg/cm^2 thick CD_2 target was placed in the center of the scattering chamber. The target purity was found to be 88% based on the ratio of elastically scattered protons and deuterons. The average beam intensity during the 10-day experiment equaled 4.1×10^6 pps, with a center-of-mass (CM) collision energy of 5.67 MeV.

B. Detection arrays and signal handling

The scattering target was surrounded by two sets of detection arrays: the T-REX charged-particle detection setup [45] and the Miniball (MB) γ array [46,47].

The T-REX charged-particle detection setup consisted of eight silicon ΔE-E telescopes (ΔE thickness, 140 μm; E thickness, 1000 μm), four in both forward and backward directions (with respect to the target), covering an angular range from 27° to 78° in the forward and from 103° to 152° in the backward direction [45]. Each telescope consisted of 16 resistive position-sensitive strips oriented perpendicular to the beam direction, to allow position determination of detected particles. Calibration of the ΔE detectors was done using a quadruple α source (^{148}Gd, ^{239}Pu, ^{241}Am, and ^{244}Cm). The shielded E_{rest} detectors were calibrated using the Compton scattering of high-energy photons from ^{60}Co and ^{152}Eu γ-ray sources detected by TREX-Miniball coincidences. Also data from stable beam reaction experiments [e.g., ^{22}Ne(d,p)^{23}Ne] was used to improve the quality of the calibration. During the calibration process it was found that the full energy signal of the ΔE detector depends on the position of the hit along the strip. All full-energy signals were hence corrected for this problem with parameters extracted from the measurement with the α source, using the relationship $E_{\text{corrected}} = E_{\text{measured}}/[1 - (0.5 - x)A]$, with $A = 0.035$ and x the normalized position along the strip ($x = [0,1]$). The global energy resolution of protons emitted in the (d,p) reaction detected by the ΔE-E telescopes was determined by the combination of intrinsic detector resolution, position uncertainty, beam-spot size, energy losses, and angular dependence of the particle kinematics, and was of the order of 1300 keV full width at half maximum (FWHM). When using α sources typical energy resolutions of 55 keV were achieved. The forward quadrants were shielded by a 12-μm Mylar foil to reduce the amount of incident elastically scattered particles at laboratory angles greater than 70°, where the incident rate was high and kinetic energy of the particles low because of the reaction taking place in inverse kinematics. The influence of the Mylar foil on the detected energy of protons resulting from a (d,p) reaction is discussed in Sec. III A. The particle detectors were divided in two trigger groups (top-left and bottom-right), with as trigger condition either a hit in the ΔE or E part in one of the quadrants of the trigger group. The 64 channels of the position sensitive strips were divided over two Mesytec MADC-32 modules (with internal time stamping) while the remaining signals (full ΔE energy and E energy) were all connected to a separate MADC-32.

Initially during the experiment a significant amount of background events was noticed in the backward quadrants of T-REX, directly proportional to the instantaneous beam intensity and target thickness. The combination of the slow extraction from REX-EBIS (see Sec. II A) and a reduction in beam intensity were necessary to control this problem, which was caused by random summing of δ electrons created by the heavy-ion beam interacting with the CD_2 target or target holder material [48].

To detect the γ rays that were emitted after the population of ^{67}Ni in an excited state, eight Miniball cluster detectors were positioned around the scattering chamber [46]. Each Miniball cluster was composed of three hyperpure germanium crystals, which were sixfold electrically segmented. The high granularity of the Miniball array allowed a precise determination of the direction of the detected γ rays, which was necessary to perform a Doppler correction of the detected γ-ray energy. This was needed as the decaying nuclei traveled at speeds around 0.08c while emitting γ rays, leading to Doppler shifts of the emitted wave lengths. The position of all clusters was determined with high accuracy by analyzing the data from the ^{22}Ne(d,p)^{23}Ne reaction with known incoming energy and by measuring the Doppler shift of the 1017-keV line for each segment. The signals from the Miniball array were digitally handled by a series of digital gamma finder (DGF) modules, with an energy range of nearly 8 MeV. Energy calibration and efficiency determination were done using ^{152}Eu and ^{207}Bi sources. For the high-energy part of the spectrum, data from the β decay of a stopped ^{11}Be beam ($T_{1/2} = 13.76$ s), including transitions up to 7.97 MeV, were used [49]. The total photopeak efficiency for 1-MeV γ transitions was found to be 5.9%. As the energy resolution of the detected protons in T-REX was insufficient to disentangle individual excited states purely based on proton kinematics, proton-γ coincidences were necessary to obtain angular distributions. A similar strategy was used in one-nucleon transfer reactions on stable nuclei to extract angular distributions for unresolved levels, like, e.g., ^{64}Zn(d,^{3}Heγ) and ^{64}Ni(d,^{3}Heγ) [50,51].

Data were acquired during the 800-μs beam ON window, during which a bunch of ions was ejected from REX-EBIS and accelerated by REX. After this window was closed, the obtained data were read out and another 800-μs beam OFF window was started, encompassing natural background and β-decay radiation of isotopes stopped in the scattering chamber. The REX duty cycle is sufficiently long to allow acquisition and readout of both windows before the next pulse. All detected signals were directly time-stamped by internal clocks running at 40 MHz.

C. Delayed-coincidence technique

In Sec. I the currently available experimental data concerning the 1007-keV $9/2^+$ isomeric state ($T_{1/2}$ of 13.3 μs) in ^{67}Ni were discussed. The μs lifetime of this state inhibits the analysis of prompt proton-γ coincidences with Miniball and thus no angular distributions based on γ gates could be produced. For this purpose a delayed-coincidence (DeCo) technique was developed encompassing a thick ($\approx 60\,\mu$m), removable aluminum foil used to stop the incoming beam and a dedicated coaxial germanium detector with the purpose of detecting the isomeric, delayed transitions of 313 and 694 keV emitted during the decay of the 1007-keV isomeric state. It should be noted that the 1007-keV isomeric state can be populated either as a result of direct population in the transfer reaction, or when an excited state with a higher excitation energy is produced which decays subsequently (promptly) to the 1007-keV isomeric state. The aluminum foil was positioned 2 m downstream of the target position and renewed every 8 h to limit the background originating from accumulating β-decaying nuclei, mainly ^{67}Cu. The coincidence window between γ rays detected in the delayed-coincidence chamber and particles detected by T-REX was asymmetrically set to 120 μs, ranging from -40 μs to 80 μs with the particle time stamp as the reference point. The time relation between the detected protons and γ rays is shown in Fig. 1 in Ref. [38] for the 313-keV transition (left and right background next to the 313-keV transition is subtracted) and shows the definition of the *delayed* and *random-delayed* windows, which are both 40-μs long. The delayed-coincidence time window hence accounts for 87.5% of the isomeric transitions. As a comparison, the time relation between γ rays detected in Miniball and protons detected in T-REX is given in Fig. 1, showing the more narrow coincidence window. In the case of Miniball-T-REX coincidences, the detected radiation is either *prompt* or *random* as defined in Fig. 1.

As the time of flight between the reaction target and the delayed-coincidence setup was of the order of 80 ns, losses from in-flight γ decays were negligible. The exponential shape has a fitted half-life of 13.7(6) μs which is in good agreement with the previously measured values of 13.3(2) μs (Ref. [26]) and 13(1) μs (Ref. [35]) and confirms the weighted average of 13.3(2) μs [26].

The efficiency of the delayed-coincidence detection setup was determined in two steps: using a calibrated ^{152}Eu point source at the position of the aluminum foil (absolute photopeak efficiency using a point source) and also by using the reaction data itself by comparing the intensities of the prompt γ transitions arriving on top of the isomer with the intensity of 313 and 694 keV in delayed coincidence with these events. The second step also includes the effect of a non-point-like source and the transmission efficiency between the reaction target and the delayed-coincidence setup. By comparing the results from both steps, this transmission efficiency could be determined. As an example, Fig. 2(a), background and random subtracted, shows the prompt Miniball radiation in delayed coincidence with either 313 keV or 694 keV, which allowed one to identify transitions arriving on top of the 1007-keV

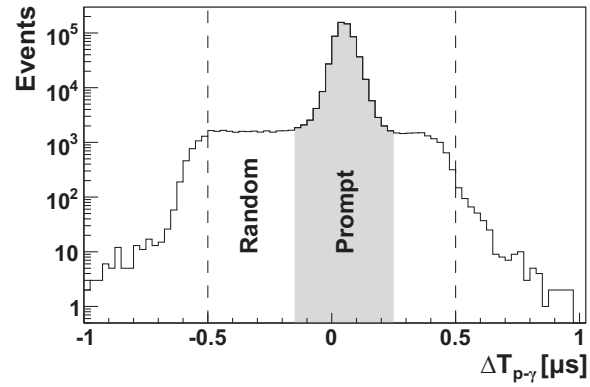

FIG. 1. Proton-γ time difference between γ rays detected in Miniball and protons detected by T-REX. The gray region defines the *prompt* proton-γ time window; other events are referred to as *random* coincidences. The width of the prompt window is determined by the timing resolution of the low-energy γ rays after the walk correction.

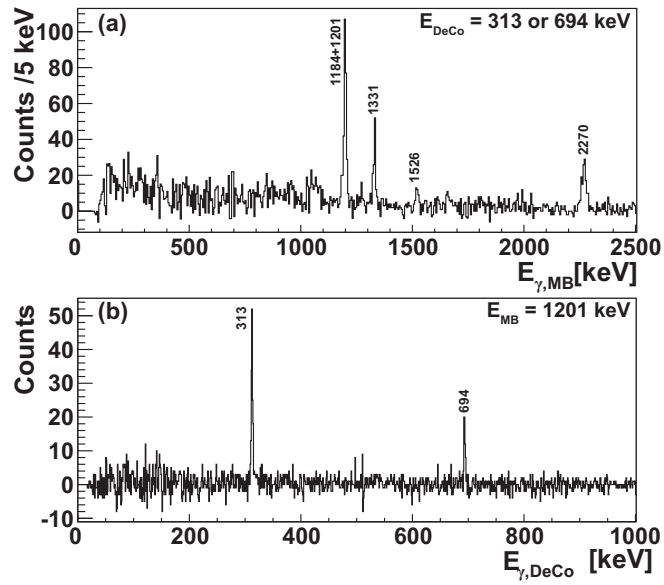

FIG. 2. (a) Doppler corrected γ-ray spectrum in Miniball, delayed coincident with either 313 keV or 694 keV. Random-delayed events (see, e.g., Fig. 1 in Ref. [38]) and the delayed coincident background have been subtracted. (b) Delayed coincidence spectrum requiring a prompt proton-1201-keV event in Miniball. This spectrum was used to determine the delayed coincidence efficiency. See text for more information.

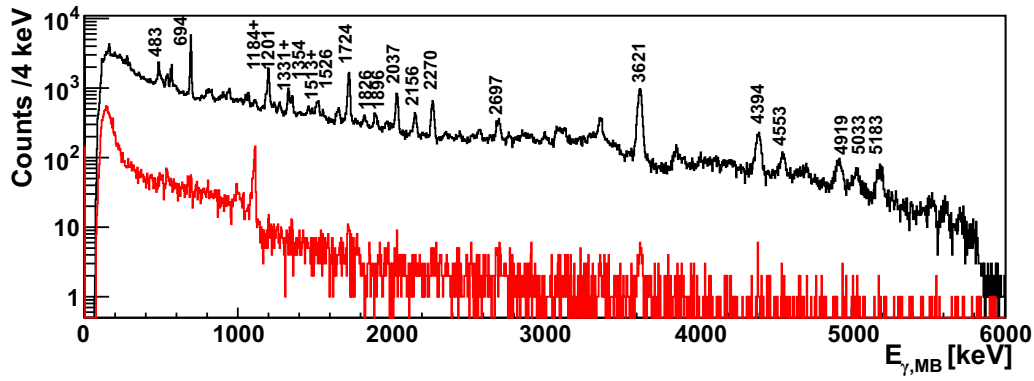

FIG. 3. (Color online) Doppler corrected Miniball γ-ray spectra, prompt proton coincident (black), and random proton coincident (red). See Fig. 1 for definition of Miniball timing windows. In the prompt spectrum most lines belonging to the γ decay of ^{67}Ni can be clearly identified, while only traces of the most intense lines remain in the random spectrum together with a broadened β-decay line around 1039 keV (^{66}Cu $\rightarrow$ ^{66}Zn). Energies of the most prominent γ rays are indicated in keV.

isomer. Figure 2(b) shows the inverse situation as the delayed-coincidence spectrum is shown, requiring a prompt 1201-keV transition in Miniball. One can compare the 1201-keV intensity in Fig. 3 depending on the gate photopeak efficiency of Miniball ($\propto \epsilon_{\mathrm{MB,1201}}$), with the intensity of either the 313- or 694-keV transitions in Fig. 2(b) which is proportional to the product of the delayed-coincidence detector photopeak efficiency, gate photopeak efficiency of Miniball, and the transmission efficiency ($\propto \epsilon_{\mathrm{DeCo,313\ or\ 694}}\ \epsilon_{\mathrm{MB,1201}}\ \epsilon_{\mathrm{Trans}}$). The integral counts of each peak are evaluated through a fit procedure (Gaussian shape). In the case of doublets (like the 1184- to 1201-keV and the 1331- to 1354-keV doublets) the fit procedure allows one to disentangle each contribution, which is then used in the efficiency calculation. The uncertainties that results from this fitting procedure are included in the obtained peak integral. The product of $\epsilon_{\mathrm{DeCo,313\ or\ 694}}$ and $\epsilon_{\mathrm{Trans}}$ defines the global efficiency for detection of the 313- or 694-keV transition in the DeCo set-up. As all parameters except the transmission efficiency were known from source data, the transmission efficiency from the target position to the delayed-coincidence detection setup could be determined. An overview of these efficiencies is given in Table I, leading to an average transmission efficiency of 53 (6)%.

III. ANALYSIS

A. Data structure

The event-by-event structure of the data allowed to construct particle-γ coincidences by placing a 1-μs coincidence window around the time stamps of the detected signals. The effective particle-γ_{MB} time structure within these events is shown in Fig. 1, indicating that the majority of the γ rays detected within 1 μs of a proton is indeed prompt radiation resulting from transfer reactions. Events outside of the $\pm$0.5-μs time window were because of higher-multiplicity events and shifts from the walk correction applied to the time stamps of low-energy γ rays. The data in the random time window of Fig. 3 were scaled based on the integrals of γ rays originating from β-decaying nuclei implanted in the detection chamber in the prompt and random time window. The prompt nature of the radiation is also evident in Fig. 3, where the corresponding γ spectra are shown for both prompt and random proton-γ timing conditions. The data in the random spectrum are limited and only contain a doubly humped structure around 1039 keV, the dominant transition in the β decay of ^{66}Cu (note that no γ rays are emitted in the β decay of ^{66}Ni) [52], in which shape is from the Doppler correction procedure. Traces of the most intense prompt transitions, Compton background of the 1039-keV transition and radiation from the REX-accelerator, are also observed.

After the event building and calibration of the raw, detected signals, the kinematic reconstruction of the events was performed. In the case of the γ rays detected by Miniball, the *add-back* procedure was performed by summing γ-ray energies detected within the same cluster. The segment in which the highest energy was deposited is chosen as the primary interaction point and provided the direction used for Doppler correction [46].

TABLE I. Overview of the efficiency of the delayed-coincidence setup for the two delayed transitions of interest with energies of 313 and 694 keV. The first row includes the absolute photopeak efficiency for the germanium detector obtained from source data. Furthermore, the global efficiency, determined using three prompt T-REX Miniball gates, is given. The weighted averages of these different gates (line 4) are used in the analysis of the data. Finally, the transmission efficiency from the comparison between the absolute photopeak efficiency with the global efficiency is shown. This transmission efficiency from the target position to the decay correlation detection setup also incorporates the fact that the spread of ions on the stopper foil is not a point source.

Gate (keV)	313 keV	694 keV
Source	7.4 (2)	4.4 (2)
1201	4.4 (5)	1.7 (5)
1331	4.6 (8)	1.8 (7)
2270	4.0 (8)	2.8 (7)
Global	4.4 (6)	2.0 (4)
Transmission	59 (8)	46 (9)

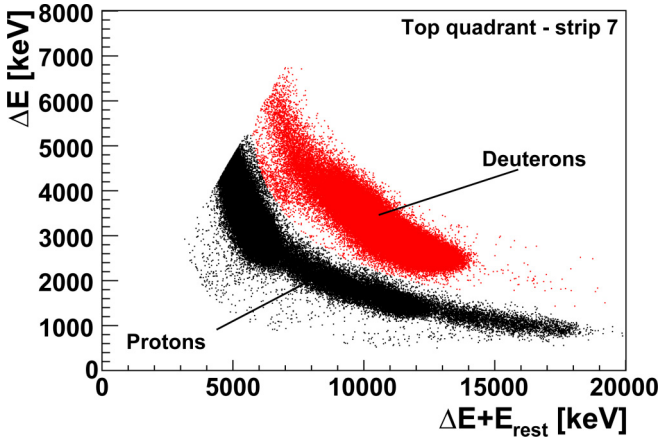

FIG. 4. (Color online) Measured ΔE-E signature in strip 7 (θ_{LAB} between 42° and 48°) of the barrel detector. Particles that are stopped in the ΔE part of T-REX are rejected and not shown in this figure. The red events correspond to particles that are identified as deuterons based on their kinematical signature by the analysis software. Alternatively, the black dots are identified as protons.

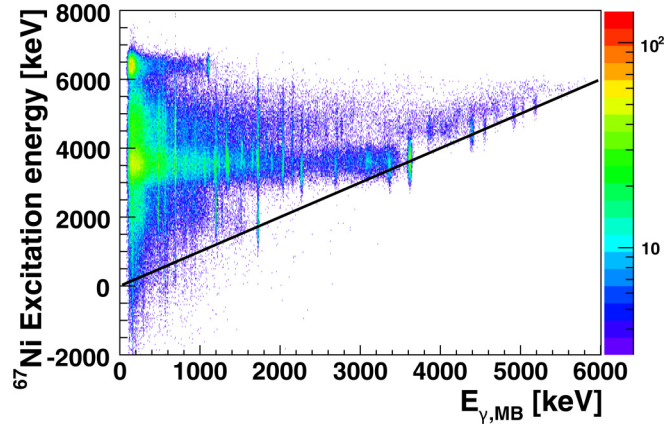

FIG. 5. (Color online) Doppler corrected energy of γ rays with respect to the original excitation energy of ^{67}Ni, deduced from proton kinematics. Events on the solid line correspond to direct ground-state γ transitions after the transfer reaction.

In the case of γ rays detected in the delayed-coincidence setup, 120-μs-wide coincidence windows were applied. Delayed-coincident γ rays could in principle be assigned to several light, charged particles (p, d, t, α, and ^{12}C) detected by T-REX within the 120-μs time window. However, the data showed that after kinematical identification (see next paragraph) 95% of the delayed-coincident γ rays were uniquely assigned to a single proton.

Particle identification was performed based on their ΔE-E signature for particles detected in the forward direction ($\theta_{\mathrm{LAB}} < 90°$). Figure 4 illustrates the separation between identified deuterons and protons in one strip of the forward ΔE-E telescope. In the backward direction all protons were stopped in the ΔE detector and hence the E_{rest} detector served as a veto to filter out electrons. Note that no elastically scattered particles are emitted in the backward direction.

Energy corrections were applied to the detected particles for energy losses in the Mylar foil (only forward direction) and target (all directions). These corrections were obtained by calculating the range of the detected particles in, e.g., the Mylar foil based on the detected energy, adding the effective thickness of the foil to this calculated range and calculating the energy needed to obtain this combined range. Finally, based on the proton kinematics (energy and position of the detected proton), the corresponding excitation energy of ^{67}Ni was calculated based on the missing mass method.

B. ^{67}Ni Level scheme

To construct the level scheme, information from (proton-) $\gamma\gamma$ coincidences, (proton-)DeCo-γ coincidences (see Fig. 2), and coincident initial excitation energy (from the missing mass method) was combined. An instructive figure combining data from Doppler corrected γ-ray energy in Miniball and initial excitation energy is shown in Fig. 5, which can be used as a first guide to construct the level scheme and determine the (order of the) decaying γ transitions. Events situated on the solid line correspond to transfer reactions that populate a specific excited state which subsequently decay by the emission of one γ ray directly to the ground state. Already from this figure one can clearly identify substantial feeding of excited states at 1724 and 3621 keV, followed by direct decay to the ^{67}Ni ground state.

The most detailed information can be obtained from the combination of proton-$\gamma\gamma$ coincidences and the corresponding incoming excitation energies. An example is given in Fig. 6(a), where proton-$\gamma\gamma$ coincidences are shown with a gate on the 1724-keV transition. Two strong transitions are clearly visible. The order of the 483-, 1724-, and 1896-keV γ rays can be determined by plotting the incoming excitation energy of ^{67}Ni deduced from the missing mass method for each of these transitions. The spectrum for 1724 keV shows multiple peaks, with the one at lowest energy around its transition energy of 1724 keV. The other gates have their first peak at higher energies, revealing that 1724 keV is a ground-state transition. These two other transitions are placed directly on top of the 1724-keV transition as the position of the first peak in their excitation energy spectrum matches the sum of 1724 keV and the γ-ray gate energies, defining two states at 2207 and 3621 keV.

Repeating this analysis for all possible γ gates allowed one to create the level and decay scheme of ^{67}Ni shown in Fig. 7. As a consistency check a comparison was made between the experimental excitation spectrum (or feeding probability) deduced from all detected protons in singles and a reconstruction based on the proposed level scheme (Fig. 7), and measured γ-ray intensities. This comparison is presented in Fig. 8. The normalization of both feeding probabilities was based on the integrals of both curves up to an energy of 5400 keV to exclude the influence of the elastic proton peak at 6.4 MeV. In the reconstructed curve the ground-state feeding was left as a free variable and a 4(1)% contribution was found based on an iterative procedure. For each state the data from the γ intensity were folded with a Gaussian distribution with FWHM of 800 keV (obtained from the experimental data). The good overall agreement between the excitation spectrum obtained from proton energies alone and the reconstructed

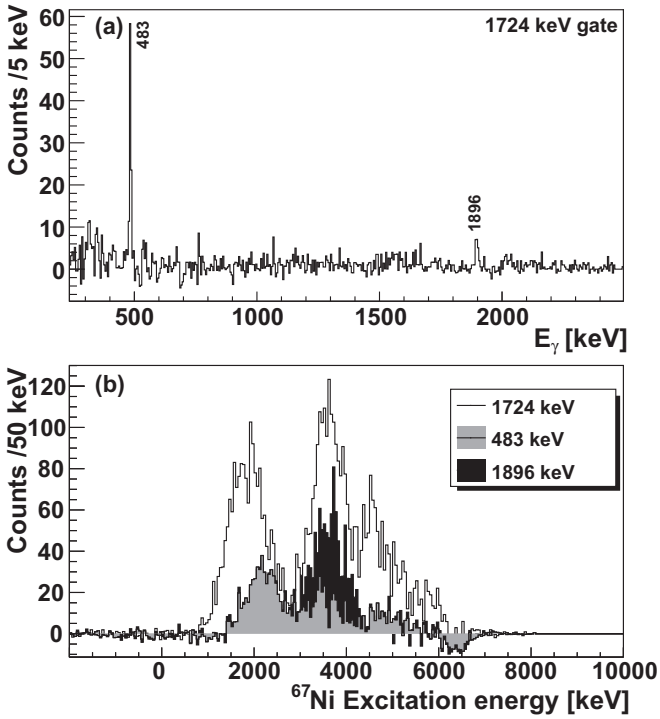

FIG. 6. (a) Proton-γ-γ coincidences for the 1724-keV transition. The strongest coincidences at 483 and 1896 keV are clearly visible. (b) Corresponding incoming excitation energies in ^{67}Ni deduced from coincident proton kinematics for 1724 keV and coincident γ rays, efficiency corrected. See text for more information.

curve based on γ intensities supports the proposed level scheme and the procedure to rely on proton-γ coincidences to extract angular distributions.

A final note should be made on the region above 4-MeV excitation energy. When searching for γ rays originating from this excitation energy in ^{67}Ni, some direct ground-state transitions can be seen, as well as most of the γ rays found at low excitation energy in the level scheme (e.g., 694, 1201, and 1724 keV), but in Fig. 5 transitions connecting these highly excited states with those at lower excitation energy are not observed. This nonobservation might be from the higher level density at high excitation energy and the large variety of possible decay paths; (d,p) experiments on lighter nickel isotopes at comparable CM energies have shown that at high excitation energy a large number of states are populated with somewhat small cross sections, supporting this statement [53–60]. The reconstructed curve in Fig. 8 for excitation energies higher than 4 MeV was corrected for this missed top-feeding by comparing the intensities of the γ rays placed in the low-energy part of the level scheme with the direct ground-state decay. From this analysis the total amount of missed γ-ray intensity was found to be 50% of the total intensity.

In Fig. 5 a strong signal above 6-MeV excitation energy can be seen, mostly random coincidences with low-energy γ rays and the 1039-keV transition (^{66}Cu β decay). This 6.4-MeV excitation-energy signature corresponds to elastically scattered protons (impurities in the target), which are in random coincidence with background radiation. This strong signature is also visible in Fig. 8 at 6.4-MeV excitation energy.

C. Normalization

To normalize the measured angular distributions and obtain absolute cross sections, the beam intensity must be known. Here elastically scattered deuterons were used to determine the beam intensity by scaling the differential elastic cross section to the experimental data as $N = It\frac{d\sigma}{d\Omega}\Delta\Omega\frac{\rho d}{A}N_A P_d \epsilon_D$, with I the average beam intensity, t the measuring time, $\frac{d\sigma}{d\Omega}$ the differential cross section, $\frac{\rho d}{A}N_A$ the number of target nuclei per unit surface, P_d the target purity, and ϵ_D the efficiency for detecting deuterons, including losses in the particle identification. This last angle-dependent parameter is obtained from GEANT4 simulations [45,61]. All these quantities except the average beam intensity are known. As the detection range for deuterons was limited from 35° to 50°, it was not possible to fit the optical potentials to the available data and hence global optical model potentials (GOMPs) have been used. Figure 9 shows the comparison of three differential cross section calculated with the program FRESCO [62] using different GOMPs available from literature [63–65], with the GOMP from Ref. [65] giving the best agreement because of the larger Coulomb radius. The most important optical model potential parameters used are summarized in Table II. A total average beam intensity of $4.1(3) \times 10^6$ pps was found using this analysis.

By normalizing the transfer data to the elastic scattering of deuterons, uncertainties in physical properties of the target can be neglected as both data sets are obtained under the same conditions and hence do not depend on the properties of the target.

D. DWBA analysis

The theoretical transfer-reaction angular distributions were calculated using the DWBA code FRESCO [62]. For the incoming channel potentials from Ref. [65] were used. As the range of identified elastically scattered protons is insufficient to fit the optical-model potentials to the data, four sets of GOMPs available from literature can be used to describe the outgoing channel [66–69]. The main difference between these sets is that the former two GOMPs include a real volume part, while the latter two don't. In this analysis the GOMPs from Ref. [66] were used, however, the shape of the angular distributions does not vary significantly between the different sets of potentials, while variations in the magnitude of the differential cross section are limited to 10%. An overview of the optical model potential parameters used can be found in Table II. To calculate the wave functions of the neutron bound in ^{67}Ni, a Woods-Saxon potential was used with standard radius and diffuseness parameters of $r = 1.25$ fm and $a = 0.65$ fm. The depth of this potential is rescaled to reproduce the correct neutron binding energy.

The low CM energy of the reaction (5.67 MeV) justifies the use of DWBA over ADWA as the influence of deuteron breakup is negligible at this CM energy [70]. The influence of nonlocality in the reaction as discussed in Ref. [71] was

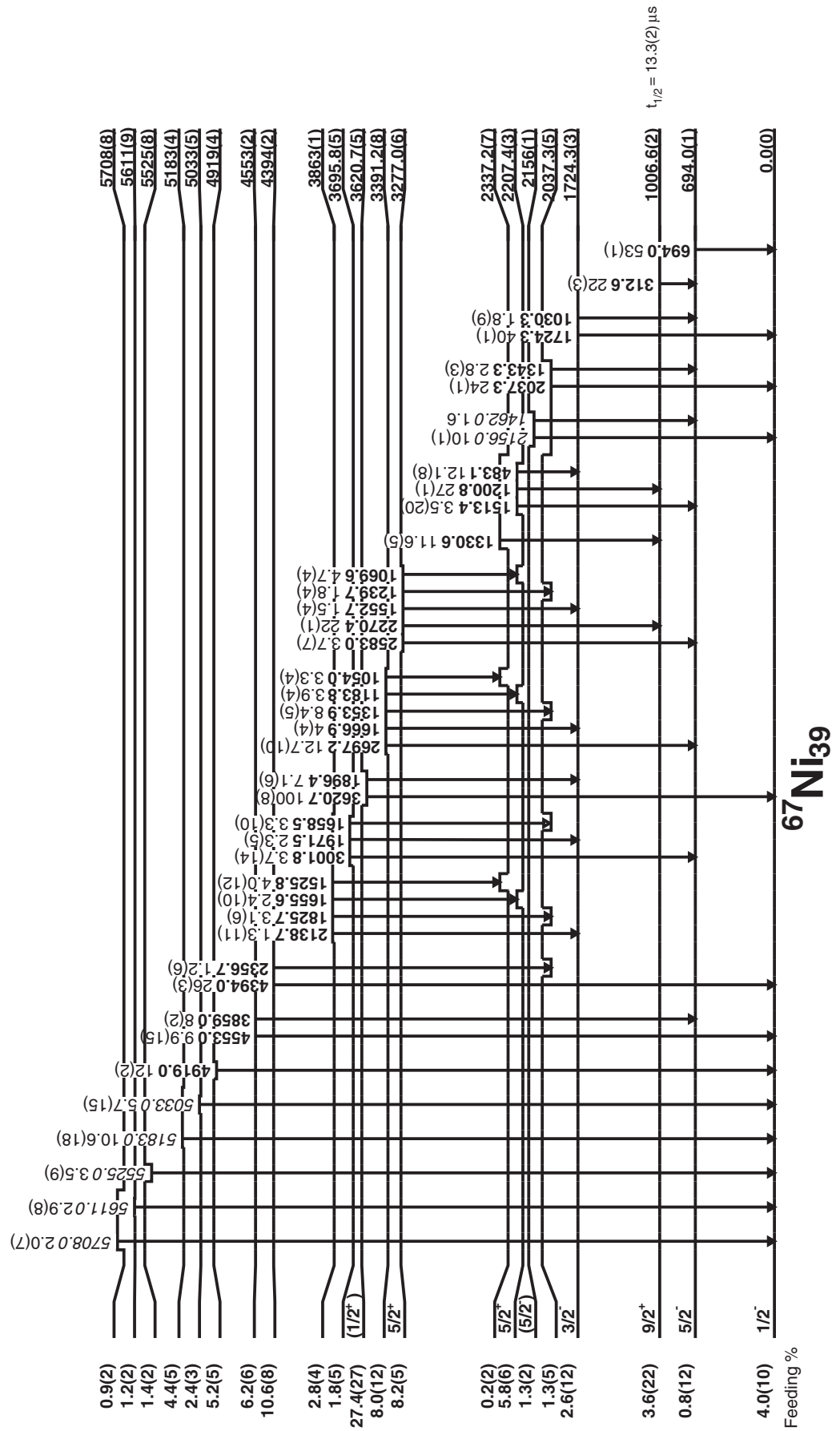

FIG. 7. Level scheme constructed from the available (d,p) data. Gamma and level energies are given in keV. Gamma-ray intensities relative to the 3621-keV transition.

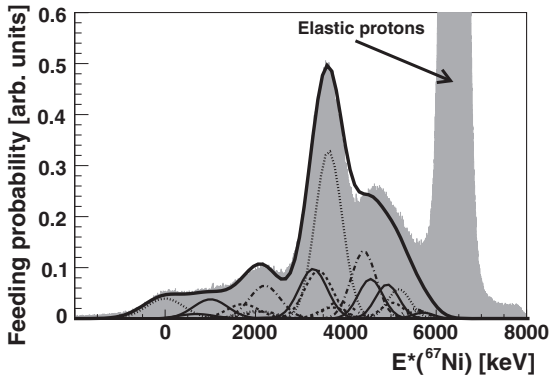

FIG. 8. Experimental excitation spectrum deduced from proton kinematics in singles (gray area) compared with a reconstructed feeding probability based on the proposed level scheme and γ-ray intensities (black line). The contribution of each individual state was drawn for completeness.

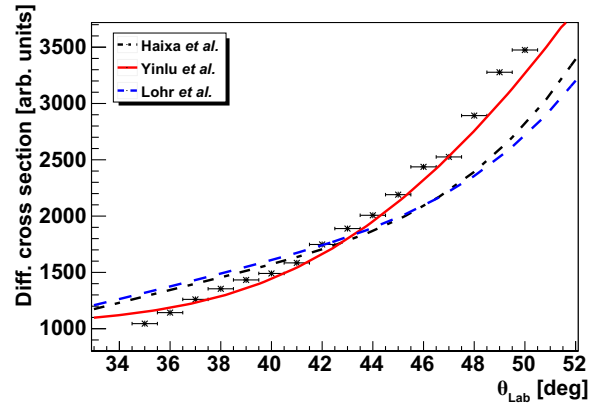

FIG. 9. (Color online) Angular distribution of elastically scattered deuterons. The DWBA calculations using optical potential paramaters from Refs. [63–65] are shown as the three lines.

assessed and limited influence on the calculated differential cross sections was found. The variations in the extracted relative spectroscopic factors from this nonlocality were found to be of the order of 10% at most and did not change the results within the quoted error bars.

As the absolute scaling factors between the calculated cross sections and the experimental data at energies near the Coulomb barrier depend both on the optical model potentials and geometry of the single-particle binding potentials, absolute spectroscopic factors (C_S^2) cannot be quoted reliably [72]. Therefore only relative spectroscopic factors (with respect to the 1007-keV isomer originating from the $\nu g_{9/2}$ orbital) and asymptotic normalization coefficients (ANCs) will be reported here. The choice for the 1007-keV state was based on the available experimental data discussed in Sec. I indicating the high spectroscopic purity of this state. Calculations for all populated states were performed assuming pure configurations (spectroscopic factor $= 1$) with angular momenta of $s_{1/2}$, $p_{1/2,3/2}$, $d_{5/2}$, $f_{5/2}$, and $g_{9/2}$.

From the experimental data, angular distributions were obtained by requiring double gates on excitation energy (proton kinematics) and coincident γ-ray energy, similar to the analysis in Ref. [51]. The width of excitation-energy window was set to 600 keV to reduce possible distortion from γ feeding from higher lying levels. By using this width, only 70% of all events were included, because the FWHM of these peaks in the excitation-energy spectra is about 800 keV. In case of a small separation between excited states, connected by an intense γ-ray transition (e.g., 1724 and 2207 keV, connected by the 483-keV transition), the contribution of the 2207-keV state was explicitly subtracted by combining spectra from different gates. A complete list of all gates used can be found in Table III. Angular distributions were obtained in the laboratory frame of reference in 5° bins, all individually efficiency corrected, with coefficients obtained from GEANT4 simulations [45,61]. Depending on the γ-decay pattern, multiple γ gates could be used to obtain an angular distribution for a specific state. In this case, the angular distributions were created for all these possible gates, including individual corrections for γ-detection efficiency, before creating the global angular distribution from the weighted average. If applicable, delayed-coincidence data were included for states decaying via the isomeric state at 1007 keV. Only for the ground state a single gate on excitation energy was used because of the lack of (delayed) coincident γ rays.

IV. RESULTS

The extracted angular distributions and comparison with DWBA calculations can be found in Fig. 10 and an overview of the extracted spectroscopic information is given in Table III, along with information from previous experiments [26,29–33,35]. States compatible with an ℓ transfer between 0 and 4 have been observed. Angular distributions could only be extracted for states up to 3621 keV. Above this excitation energy the kinetic energy of the emitted protons in the backward direction (small CM angles) becomes low and

TABLE II. Overview of the optical model parameters used in the DWBA analysis taken from GOMPs in Refs. [65] (incoming channel) and [66] (outgoing channel).

Channel	V	r	a	W	r_w	a_w	W_d	r_d	a_d	r_c
$d + ^{66}$Ni	(MeV)	(fm)	(fm)	(MeV)	(fm)	(fm)	(MeV)	(fm)	(fm)	(fm)
	83.4	1.17	0.81	0.7	1.33	0.47	13.9	1.563	0.7	1.35
	V	r	a	W_d	r_d	a_d	V_{so}	r_{so}	a_{so}	r_c
	(MeV)	(fm)	(fm)	(MeV)	(fm)	(fm)	(MeV)	(fm)	(fm)	(fm)
$p + ^{67}$Ni	56.7	1.20	0.67	8.33	1.28	0.48	5.72	1.03	0.59	1.25

TABLE III. Available spectroscopic information of the observed excited states in ^{67}Ni. The second column shows the γ rays used as gates to obtain the angular distribution. In case no unambiguous ℓ assignment could be made based on the measured differential cross section, all possible values have been included in column 4. The underlined value is the adopted one based on additional spectroscopic information. If available, information from Refs. [29–31] was included for the observed levels.

E_{ex} (keV)	Gates E_γ (keV)	J^π	ℓ	Rel. S.F.	ANC	σ_{tot} (mb)	Prev. exp. (E_{ex}, J^π)		
							[29]	[30]	[31]
0	–	$1/2^-$	1	1.3 (4)	3.5		0, $(1/2)^-$	0	0, $(1/2)^-$
694	694	$5/2^-$	1, 2, (3)	0.30 (9)	0.6	0.64	694, $(5/2)^-$	720	770, $(9/2)^+$
1007	DeCo	$9/2^+$	3, 4	1.0 (3)			1007, $(9/2)^+$	1020	1140, $(3/2)^-$
1724	1724	$3/2^-$	1	0.18 (5)	2.5	2.85		1710	1970, $(3/2)^-$
2037									
2156							2155, $(5/2)^-$		
2207	1201, 483, DeCo	$5/2^+$	1, 2	0.25 (7)	0.6	4.6			
2337									
3277	1070, 2270, 2583, DeCo	$5/2^+$	1, 2	0.28 (9)	0.2	6.8			
3392	2697, 1354, 1184, 1054		(0,2)	0.22 (9)		6.4			
3621	3621, 1896	$(1/2^+)$	(0), 1, 2	1.1 (4)		30.6			3680, $(3/2)^-$
3696	3001, 1658		(0,2)	0.06 (2)		2.06			
3863	1826, 1656, 1525		(0,2)	0.10(4)		4.03			
4394	4394, 2357		(0,2)	0.14(5)		8.7			
4553	4553, 3859		(0,2)	0.12(4)		6.3			
4919	4919		(0,2)	0.08(3)		4.5			
5033	5033		(0,2)	0.04(2)		2.2			
5183									
5525									
5611									
5708									

the proton energies drop below the detection threshold. In the forward direction the range becomes more confined as these protons have insufficient energy to leave a ΔE-E signature. Hence only large CM angles can be used for these states making ℓ assignments cumbersome. The combination of angular momentum fits and information from γ-branching ratios allowed one to fix spin and parities of seven excited states.

Based on allowed β decay to the $3/2^-$ ground state of ^{67}Cu (log $ft \sim 4.7$), a tentative spin assignment of $(1/2^-)$ was made for the ^{67}Ni ground state [73]. This assignment is further supported in the quasielastic reaction work of Ref. [31] where the observed angular distribution fits with a $(1/2^-)$ spin. A $(1/2^-)$ spin is also compatible with shell-model predictions. Based on the work of Zhu *et al.* the spin of the ground state

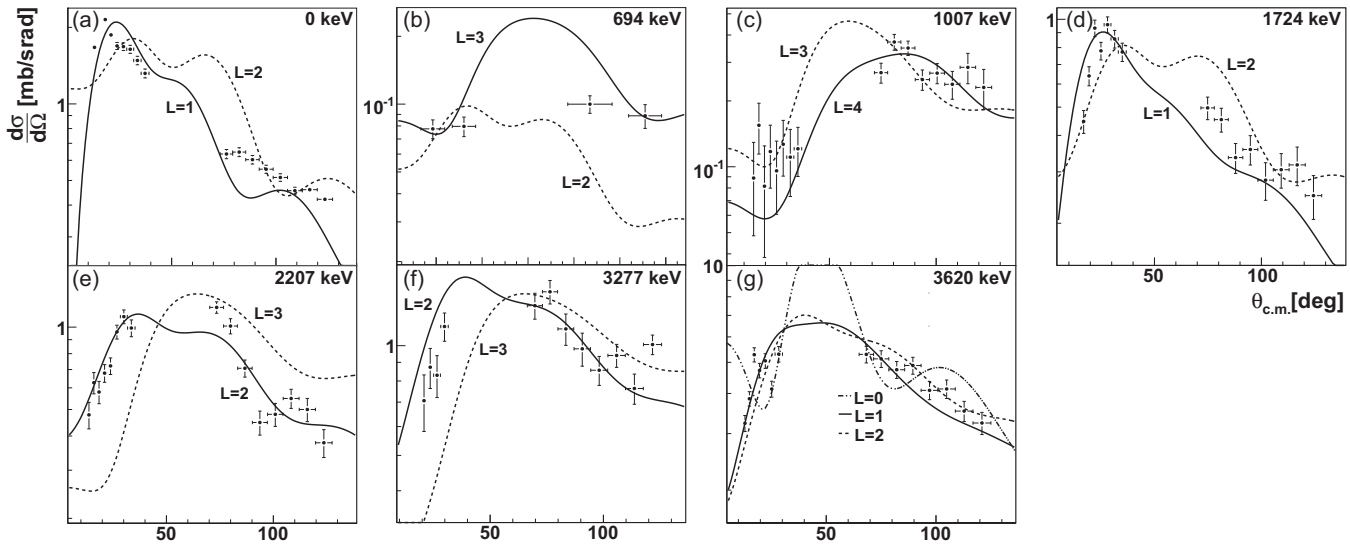

FIG. 10. Experimental angular distributions for different states in ^{67}Ni. The two or three best fits are presented for each case (solid line for best fit, dashed line for second best, and dotted-dashed for third best).

can be firmly fixed to $1/2^-$ [33]. The measured proton angular distribution in the current (d,p) experiment shows a peak near 20° in the CM frame of reference, in good agreement with an $\ell = 1$ transfer, supporting the $1/2^-$ assignment. However, no distinction can be made between $1/2^-$ and $3/2^-$ based on the transfer-reaction data alone. Assuming a $\nu p_{1/2}$ configuration for the ground state, the relative spectroscopic factor is compatible with 1 (0.5 in case of $\nu p_{3/2}$), indicating a significant single-particle contribution to the wave function. This was already suggested from the measurement of the magnetic moment of the ground state, where a value deviating by only 6% from that of a pure configuration was found [34]. For the proton angular distribution of the ground state, only a single gate on excitation energy was required. Because of the limited energy resolution, the proton angular distribution can be distorted by both the 694- and the 1007-keV state, leading to an overestimation of the differential cross section and hence also of the relative spectroscopic factor.

The first excited state at 694 keV is weakly populated and the observed proton angular distribution fits with $\ell = 1$, 2, and 3. The allowed β decay from the $(7/2^-)$ ground state of ^{67}Co provided a log-ft value compatible with a $\nu f_{5/2}^{-1}$ configuration proposed in Ref. [29]. Furthermore, several arguments support a spin and parity assignment of $5/2^-$ for this state: Recent deep-inelastic scattering work has shown that the 694- to 313-keV sequence has a stretched quadrupole character [33] which, combined with the measured lifetimes, fixes the spin of the 694-keV state to be $5/2^-$. As a final remark it should be noted that the small relative spectroscopic factor assuming a $\nu f_{5/2}$ configuration for this state is indeed expected as the $\nu f_{5/2}$ orbital is presumed to be almost fully occupied in ^{66}Ni.

The excited state at 1007 keV agrees with an $\ell = 3$ ($\chi^2_{\text{red}} = 2.4$) or $\ell = 4$ ($\chi^2_{\text{red}} = 1.8$) transfer. This state had previously been assigned a $(9/2^+)$ based on its isomeric features and similarities with ^{65}Fe [26]. The isomeric features, stretched quadrupole character of the 313- to 694-keV sequence and absence of a ground-state transition favor an $\ell = 4$ description, resulting in a delayed 313-keV $M2$ transition and spin and parity assignment of $9/2^+$. As this isomeric state decays via a cascade of two delayed γ rays, the only way to obtain a proton angular distribution was to use the delayed-coincidence technique.

In the work of Ref. [31] excited states with energies in the vicinity of the 694-keV and 1007-keV states reported here were observed. However, the spin assignments for these states are reversed and for the 1007-keV isomer a spin of $3/2^-$ was proposed. When the ejectile angular distribution for the 1140-keV state in Ref. [31] is compared with the calculation for a $9/2^+$ spin of the 770-keV state, the agreement is very reasonable when taking into account that all quoted excitation energies in Ref. [31] have an offset compared to the values reported here.

In the case of the 1724-keV level the observed angular distribution of the transfer protons is in good agreement with an $\ell = 1$ transfer. A spin and parity assignment of $3/2^-$ is preferred for two reasons. First, strong top feeding from the $5/2^+$ level at 2207 keV ($E_\gamma = 483$ keV; see below) is observed where the inclusion of an $E1$ component is necessary as a pure $M2$ transition in the case of spin $1/2^-$ would be too slow to explain this strong γ branch. Secondly, there is the small γ-ray branch to the $5/2^-$ state at 694 keV, with an observed ratio of branching ratios $I(1030)/I(1724) = 0.05$. Using Weisskopf estimates the theoretical branching ratios would be 8×10^{-5} for $1/2^-$ (respectively, $E2$ and $M1$ transitions) and 0.2 for $3/2^-$ (twice $M1$) spin and parity of the 1724-keV state. This argument supports the $3/2^-$ spin assignment for this excited state.

The proton angular distribution of the excited state at 2207 keV fits well with both $\ell = 1$ and 2. Because of the strong γ-decay link with the $9/2^+$ state at 1007, an $\ell = 2$ interpretation is favored. A spin and parity of $5/2^+$ is strongly supported by the observed γ-branching ratios to the $9/2^+$ at 1007 keV, $5/2^-$ at 694 keV, $3/2^-$ at 1724 keV, and the absence of a direct connection with the $1/2^-$ ground state which rules out a $3/2^+$ assignment. The observed branching ratios towards the $3/2^-$ and $5/2^-$ states were used to make estimates of the $B(E1)$-transition rates to these negative parity states, assuming a single-particle $d_{5/2}$-$g_{9/2}$ $E2$ transition. The obtained $B(E1)$ estimates are of the order of 10^{-4}–10^{-6}, which are typical values for this mass region [74].

The 3277-keV state has the same characteristics as the 2207-keV state. The angular distribution of the transfer protons is best described by $\ell = 1$ or 2 and this state lacks a direct ground-state transition. Because of this and in combination with a strong link with the $9/2^+$ state at 1007 keV, a $5/2^+$ spin assignment is adopted. Again, deduced $B(E1)$ values for transitions to negative parity states are of the order of magnitude around 10^{-5}, resulting in a similar interpretation as that of the 2207-keV state.

In contrast with (d,p) experiments on lighter nickel isotopes, no states with $\ell = 0$ character were unambiguously observed here, as their differential cross section strongly peaks for small CM angles where no experimental data are available. The angular distribution of the state at 3621 keV is best fitted with $\ell = 1$ or 2, but $\ell = 0$ cannot be totally discarded. As this state is only bound by 2.2 MeV, the calculated angular distributions do not show a strong ℓ dependence. Another feature is the peculiar γ decay of this state, with a strong branch to the $1/2^-$ ground state and weaker branch (7%) to the $3/2^-$ state at 1724 keV, favoring a low spin assignment for this state. The expected branching to the 1724-keV $3/2^-$ state for single-particle $M1$ or $E1$ transitions is 14%, in line with the observed value. If the spin was 3/2 or higher, one would expect to observe γ transitions towards 3/2 and 5/2 states at lower excitation energy. These have not been observed and thus the characteristic γ-decay path together with the information from the angular distribution limits the spin of this state to 1/2. In comparison with the lighter nickel isotopes, negative parity states are only observed at low excitation energy, while the excitation spectrum at higher energy is dominated by $\ell = 0$, 2, and 4 transfers. The characteristic γ decay of an identified $1/2^+$ state in ^{61}Ni exclusively decays towards $1/2^-$ and $3/2^-$ states [75]. In the ^{70}Zn(^{4}He,^{7}Be)^{67}Ni work of Ref. [31] a state at 3.680 MeV is identified with proposed spin and parity of $(3/2^-)$. However, the authors note that the angular distribution is not very characteristic. Additionally,

a difference in excitation energy quoted in [31] and this work can be noted. In the present experiment γ-ray energies were used to determine the excitation energies, which is more accurate compared to excitation energies from scattered particles. Finally, the relative spectroscopic factor for a $\nu p_{1/2}$ interpretation for the 3621-keV state would be close to 2, which is unphysically large. The combination of all these arguments favors a $(1/2^+)$ assignment for the 3621-keV state.

For the other states included in the level scheme, no angular distributions could be extracted either because of limited statistics or confined angular range (mainly for excited states above 3.6 MeV). From a comparison with both lighter nickel isotopes [53–60] and odd-Z, even-N nuclei near the semimirror nucleus $^{90}_{40}Zr_{50}$, where protons occupy the same orbitals as the neutrons do around ^{68}Ni, it is expected that nearly the full pf strength is exhausted in the observed states at low excitation energy [76–78]. In ^{62}Ni$(d,p)^{63}$Ni and ^{64}Ni$(d,p)^{65}$Ni reactions [57–59] ℓ values above 3 MeV are all identified as 0 or 2 and limited contributions of 4. At these excitation energies, the integrated calculated cross sections within the detectable range for $s_{1/2}$ ($\ell = 0$) and $d_{5/2}$ ($\ell = 2$) are nearly identical and hence also their relative spectroscopic factors are similar. As no conclusion can be drawn on their spin, these states are indicated as (0,2) in Table III as they are expected to exhibit $\nu s_{1/2}$ or $\nu d_{5/2}$ single-particle strength from systematics.

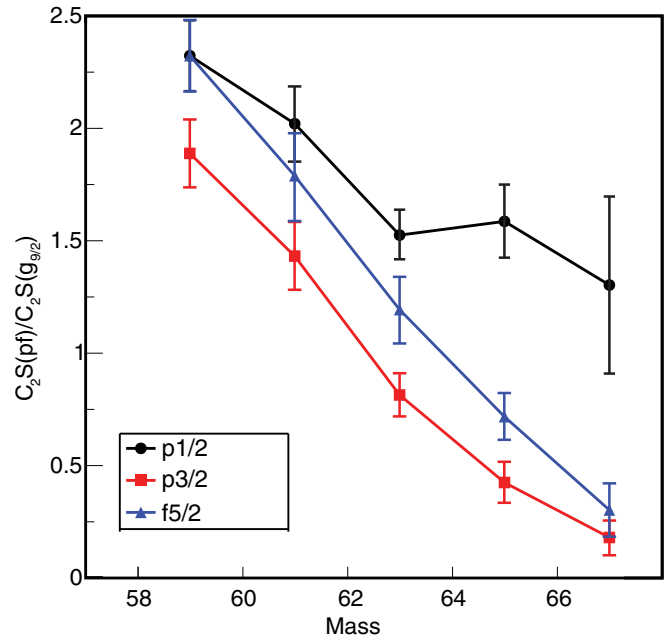

FIG. 11. (Color online) Sum of the $\nu p_{1/2}$, $p_{3/2}$, and $f_{5/2}$ spectroscopic factors relative to $\nu g_{9/2}$. See text for discussion. Data from [79,80].

V. DISCUSSION

A. Distribution of the single-particle strength

The overview of extracted relative spectroscopic factors (relative to the 1007-keV $9/2^+$ isomer) can be found in Table III and is visualized in Fig. 13(a). The relative spectroscopic factor of the $1/2^-$ ground state, which is compatible with 1, indicates that the $\nu p_{1/2}$ and $\nu g_{9/2}$ orbitals in ^{66}Ni are nearly equally empty and is consistent with the measured magnetic moment of the ground state which is close to the Schmidt value [34]. Furthermore, the experimental relative spectroscopic factors of the $5/2^-$ state at 694 keV and the $3/2^-$ state at 1724 keV, with proposed $\nu f^{-1}_{5/2}$ and $\nu p^{-1}_{3/2}$ configurations, respectively, are also small, but not zero. This hints towards a limited amount of neutron pair scattering across the $N = 40$ shell gap. A recent application of the sum rule [81], combining (d,p) and (p,d) reaction data on the stable even-A nickel isotopes, allowed one to extract the neutron orbital occupancies in these isotopes [79,80]. In the case of ^{64}Ni, the heaviest stable isotope, already a 54% occupation of the $\nu p_{1/2}$ orbital is observed, along with a limited occupation of 6.6% of the $\nu g_{9/2}$ orbital. In Fig. 11, the sum of the spectroscopic factors of the neutron addition reaction (d,p) on $^{62-64}$Ni for the $\nu p_{1/2}$, $p_{3/2}$, and $f_{5/2}$ orbitals relative to $g_{9/2}$ are shown as deduced from [79,80]. The downward trend, observed for the $p_{3/2}$ and $f_{5/2}$ orbitals when moving towards heavier nickel isotopes, continues in ^{67}Ni and indicates the steady filling of these orbitals in the even-even nickel when moving from the $N = 28$ towards the $N = 40$ shell closures. However, for the $p_{1/2}$ orbital, from ^{63}Ni onwards, a deviation from the general downward trend is observed. This indicates an increasing neutron occupancy of the $g_{9/2}$ orbital, possibly combined with a similar occupancy of the $p_{1/2}$ in ^{64}Ni and ^{66}Ni (see Fig. 3 from [79]).

The two $\ell = 2$ states at 2207 and 3277 keV have both been assigned a $5/2^+$ spin and parity. From Table III it is clear that both states contain a nearly equal amount of $\nu d_{5/2}$ single-particle strength, accounting in total for 54(11)% of the observed $\nu g_{9/2}$ single-particle strength. Such twofold splitting is also observed in (d,p) reactions on ^{58,60,62,64}Ni from Refs. [53–60], with a total strength of 31%, 27%, 23%, and 34%, respectively. In those experiments a larger number of $5/2^+$ states was observed, but in all cases a considerable part of the $\nu d_{5/2}$ single-particle strength is concentrated in two low-lying $5/2^+$ states. Because of the rise in the Fermi surface, the energy of the positive parity $5/2^+$ and $9/2^+$ states relative to the negative parity ground state in the $^{59-67}$Ni isotopes decreases steadily.

Possible configurations which can form $5/2^+$ states at low excitation energy are a pure $\nu d_{5/2}$ excitation, a $\nu g_{9/2}$ neutron coupled to a ^{66}Ni core excitation ($\nu g^1_{9/2} \otimes 2^+_{\text{core}}$), $\nu g^3_{9/2}$ configuration, and a pf neutron coupled to a core octupole excitation ($\nu pf \otimes 3^-_{\text{core}}$). The one-neutron transfer reaction is mainly sensitive to the first type of configuration as the latter two include multiparticle rearrangements. In one-neutron transfer reaction studies on lighter stable nickel isotopes using similar beam energies, the population of states with higher seniority was observed [58]. The cross section for this kind of higher-order transfer reaction is considerably weaker than the direct reactions, in most cases by orders of magnitude (see, e.g., Table 3 in Ref. [58]). Therefore it is assumed that multiparticle rearrangements do not disturb the expected and measured cross sections in the data presented here. Furthermore, in the work of Ref. [33] a collection of high-spin positive parity states

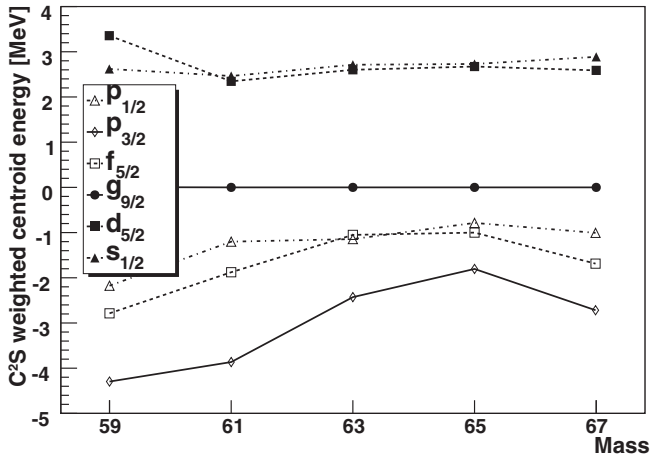

FIG. 12. Evolution of C_S^2 weighted centroid energies in the nickel isotopes with respect to the $\nu g_{9/2}$ level. Data taken from [53–60] for $^{59-65}$Ni.

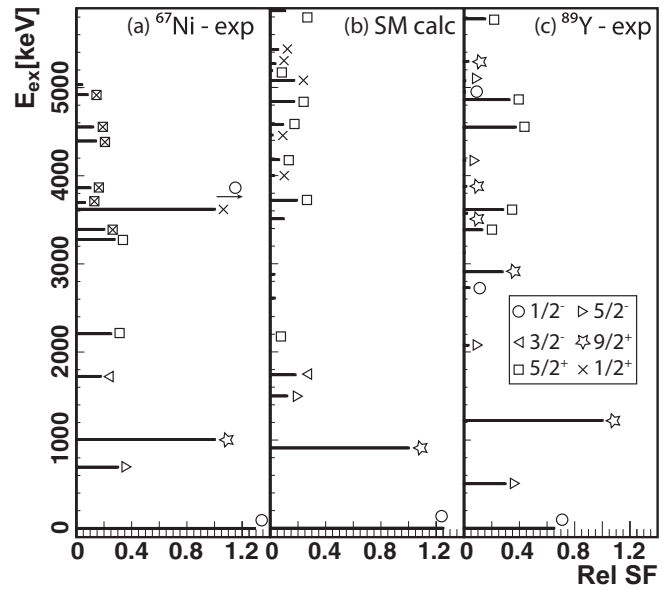

FIG. 13. Distribution of neutron single-particle strength in ^{67}Ni (experimental and shell-model calculations) and proton-single particle strength in ^{89}Y. See text for additional information.

interpreted as $\nu g_{9/2}^3$ configurations was observed. None of these states are observed in the present (d,p) data, supporting the identification of $\nu d_{5/2}$ single-particle strength in these $5/2^+$ states.

Within the present work two $5/2^+$ states with an equal and considerable amount of $\nu d_{5/2}$ single-particle strength were observed. This might hint that substantial mixing occurs between the pure $\nu d_{5/2}$ single-particle configuration and core coupled collective modes such as those discussed earlier. The amount of mixing and distribution of the different configurations over the resulting states depends on the initial energy of the unperturbed configurations. The energy of the $\nu g_{9/2} \otimes 2^+_{\text{core}}$ configuration should lie roughly 1.4 MeV above the 1007-keV $9/2^+$ state, while the calculations in Ref. [24] estimate the $\nu g_{9/2}$-$d_{5/2}$ gap to be around 1.5–2 MeV. Hence a sizable amount of configuration mixing can indeed be expected.

The C_S^2-weighted energy centroid from the neutron addition reactions for the observed states relative to the $g_{9/2}$ orbital are shown in Fig. 12, using the following expression:

$$\epsilon_j = \frac{\sum_j C_S^2 E_j}{\sum_j C_S^2}.$$

To estimate the $N = 50$ gap size in the nickel isotopes, the data from Refs. [53–60] were combined with the present set. The more recent data on the stable nickel isotopes [79,80] only include the strength of the $\nu g_{9/2}$ configuration and the negative parity states. Moreover, two assumptions were made: (1) All $\ell = 2$ states observed in $^{59-65}$Ni are $5/2^+$ states. (2) In the case of ^{67}Ni all observed states above 3 MeV are of the $\ell = 2$ character. It should be stressed here that only 50% of the available $\nu d_{5/2}$ single-particle strength is unambiguously identified, assuming the full $\nu g_{9/2}$ single-particle strength is exhausted in the 1007-keV state. The value of the $N = 50$ gap derived from these experimental data is 2.6 MeV which is in agreement with the value used in the Hamiltonian of Refs. [19,82], however, the calculated $d_{5/2}$ single-particle strength distribution seems to have been shifted by roughly 1 MeV compared to the experimental findings [see Fig. 13(b)].

The 3621-keV state with proposed spin and parity of $(1/2^+)$ and a relative spectroscopic factor of 1.1 shows a different distribution of the $\nu s_{1/2}$ single-particle strength in ^{67}Ni in comparison with the lighter nickel isotopes. In ^{62,64}Ni$(d,p)^{63,65}$Ni experiments the largest relative spectroscopic factor observed for a $1/2^+$ state is 0.4, and in general the $\nu s_{1/2}$ single-particle strength is mostly fragmented [57–59].

B. Comparison with ^{90}Zr region

The region around ^{90}Zr ($Z = 40, N = 50$) is often compared to the ^{68}Ni region ($Z = 28$, $N = 40$) as the protons in the former are expected to occupy the same shell-model orbitals as the neutrons in the latter. The level structure in ^{68}Ni and ^{90}Zr indeed looks similar. One-proton transfer data have been obtained from the ^{88}Sr(^{3}He,d)^{89}Y reaction [76] and direct comparison with our data is made [Fig. 13(c)]. Here the uncharacterized states above 3 MeV in ^{67}Ni are labeled as both $\ell = 0$ and 2. A good agreement for the negative parity pf states below 2 MeV and the $9/2^+$ state can be seen, except for the position of the $5/2^-$ state. This shift towards higher energy in ^{89}Y can be attributed to the attractive $\pi f_{5/2}\nu g_{9/2}$ tensor interaction, not present in ^{67}Ni, binding the $\pi f_{5/2}$ orbital more tightly. The ground-state relative spectroscopic factors are also similar. Data from the ^{88}Sr(d,^{3}He)^{87}Rb reaction have shown indications of a one-neutron occupancy in the $\pi g_{9/2}$ orbital in the ground state of ^{88}Sr [83].

However, a major difference in the structure of the positive parity sd states is visible as the $\ell = 0$ and 2 strength is more fragmented and resides at higher energy in ^{89}Y while the $\nu d_{5/2}$ and $\nu s_{1/2}$ strength is concentrated and shifted to lower excitation energies in ^{67}Ni. In ^{89}Y, beside these $5/2^+$

states carrying single-particle strength, a low-lying $5/2^+$ state at 2222 keV was observed, which is, however, only very weakly populated in the (^{3}He,d) reaction [76]. Also, this state can be reproduced by shell-model calculations omitting the $\pi d_{5/2}$ orbital in the valence space supporting a $\pi g_{9/2} \otimes 2^+_{\rm core}$ interpretation [84]. This distinction in the structure of the positive parity states in ^{89}Y and ^{67}Ni indicates a weaker $N = 50$ gap near ^{68}Ni compared to the $Z = 50$ gap near ^{90}Zr. The fact that in the ^{66}Ni$(d,p)^{67}$Ni experiment sizable $\nu d_{5/2}$ single-particle strength is found at low excitation energy (relative to the $9/2^+_1$ state) indicates the difference between these two regions and supports the importance of the $\nu d_{5/2}$ orbital on the nuclear structure in the vicinity of ^{68}Ni. From the distribution of the $\ell = 2$ single-particle strength in ^{89}Y the $Z = 50$ gap size is estimated to be 3.9 MeV, which is indeed 1.3 MeV larger than the $N = 50$ shell gap near ^{68}Ni.

VI. CONCLUSIONS

A one-neutron transfer reaction using a radioactive ^{66}Ni beam accelerated to an energy of 2.95 MeV per nucleon was successfully performed at the REX-ISOLDE facility in CERN, using the T-REX and Miniball arrays in combination with a delayed-coincidence setup used to perform spectroscopy of the 1007-keV 13.3-μs isomer. Excited states up to 5.8 MeV were populated in the reaction and the level scheme of ^{67}Ni was extended up to this excitation energy. DWBA analysis was performed to characterize the measured differential cross sections of the populated excited states. Negative-parity pf states were observed at energies of 0, 694, and 1724 keV. Furthermore, the $\nu g_{9/2}$ character of the 1007-keV isomer was confirmed and two $5/2^+$ states on top of this isomer were identified. The trend of the spectroscopic factors and C^2_S weighted centroids relative to the $\nu g_{9/2}$ orbital observed in previous work for $^{59-65}$Ni is continued in ^{67}Ni. The measured relative spectroscopic factors for the $5/2^+$ states show that half of the $\nu d_{5/2}$ single-particle strength is split in nearly equal parts over these two $5/2^+$ states, hinting to substantial mixing of the $\nu d_{5/2}$ configuration with collective core coupled modes. The estimated size of the $N = 50$ gap in ^{67}Ni was found to be 2.6 MeV, which shows no deviation from the gap size determined in the lighter $^{59-65}$Ni isotopes.

ACKNOWLEDGMENTS

This work was funded by FWO (Fonds Wetenschappelijk Onderzoek - Vlaanderen) (Belgium), GOA/2010/010 (BOF KU Leuven), the Interuniversity Attraction Poles Programme initiated by the Belgian Science Policy Office (BriX network P7/12), the European Commission within the Seventh Framework Programme through I3-ENSAR (Contract No. RII3-CT-2010-262010), the European Research Council (Grant No. ERC-2011-AdG-291561-HELIOS), the Slovak Research and Development Agency (Grant No. APVV-0105-10), BMBF under Contracts No. 06KY9136I, No. 05P12PKFNE, No. 06MT7178, and No. 06MT9156, and the Maier-Leibnitz-Laboratorium, Garching.

[1] O. Sorlin *et al.*, Phys. Rev. Lett. **88**, 092501 (2002).
[2] N. Bree *et al.*, Phys. Rev. C **78**, 047301 (2008).
[3] R. Broda *et al.*, Phys. Rev. Lett. **74**, 868 (1995).
[4] O. Perru *et al.*, Phys. Rev. Lett. **96**, 232501 (2006).
[5] M. Hannawald *et al.*, Phys. Rev. Lett. **82**, 1391 (1999).
[6] J. M. Daugas *et al.*, Phys. Rev. C **83**, 054312 (2011).
[7] O. Sorlin *et al.*, Eur. Phys. J. A **16**, 55 (2003).
[8] M. Sawicka *et al.*, Eur. Phys. J. A **16**, 51 (2003).
[9] J. Ljungvall *et al.*, Phys. Rev. C **81**, 061301 (2010).
[10] W. Rother *et al.*, Phys. Rev. Lett. **106**, 022502 (2011).
[11] C. Fransen *et al.*, J. Phys.: Conf. Ser. **312**, 092025 (2011).
[12] J. Van de Walle *et al.*, Euro. Phys. J. A **42**, 401 (2009).
[13] T. Baugher *et al.*, Phys. Rev. C **86**, 011305 (2012).
[14] A. Gade *et al.*, Phys. Rev. C **81**, 051304 (2010).
[15] N. Hoteling *et al.*, Phys. Rev. C **82**, 044305 (2010).
[16] S. Lunardi *et al.*, Phys. Rev. C **76**, 034303 (2007).
[17] T. Otsuka, T. Suzuki, R. Fujimoto, H. Grawe, and Y. Akaishi, Phys. Rev. Lett. **95**, 232502 (2005).
[18] A. P. Zuker, J. Retamosa, A. Poves, and E. Caurier, Phys. Rev. C **52**, R1741 (1995).
[19] S. M. Lenzi, F. Nowacki, A. Poves, and K. Sieja, Phys. Rev. C **82**, 054301 (2010).
[20] H. L. Crawford *et al.*, Phys. Rev. Lett. **110**, 242701 (2013).
[21] E. Caurier, F. Nowacki, and A. Poves, Eur. Phys. J. A **15**, 145 (2002).
[22] A. Poves, E. Caurier, F. Nowacki, and K. Sieja, Phys. Scr. **2012**, 014030 (2012).
[23] T. Otsuka, T. Suzuki, J. D. Holt, A. Schwenk, and Y. Akaishi, Phys. Rev. Lett. **105**, 032501 (2010).
[24] K. Sieja and F. Nowacki, Phys. Rev. C **85**, 051301 (2012).
[25] J. Duflo and A. P. Zuker, Phys. Rev. C **59**, R2347 (1999).
[26] R. Grzywacz *et al.*, Phys. Rev. Lett. **81**, 766 (1998).
[27] S. Rahaman *et al.*, Eur. Phys. J. A **34**, 5 (2007).
[28] R. Ferrer *et al.*, Phys. Rev. C **81**, 044318 (2010).
[29] L. Weissman *et al.*, Phys. Rev. C **59**, 2004 (1999).
[30] R. T. Kouzes, D. Mueller, and C. Yu, Phys. Rev. C **18**, 1587 (1978).
[31] M. Girod, P. Dessagne, M. Bernas, M. Langevin, F. Pougheon, and P. Roussel, Phys. Rev. C **37**, 2600 (1988).
[32] T. Pawłat *et al.*, Nucl. Phys. A **574**, 623 (1994).
[33] S. Zhu *et al.*, Phys. Rev. C **85**, 034336 (2012).
[34] J. Rikovska *et al.*, Phys. Rev. Lett. **85**, 1392 (2000).
[35] G. Georgiev *et al.*, J. Phys. G: Nucl. Part. Phys. **28**, 2993 (2002).
[36] H. Mach *et al.*, Nucl. Phys. A **719**, C213 (2003).
[37] M. Wang, G. Audi, A. Wapstra, F. Kondev, M. MacCormick, X. Xu, and B. Pfeiffer, Chinese Phys. C **36**, 1603 (2012).
[38] J. Diriken *et al.*, Phys. Lett. B **736**, 533 (2014).
[39] N. R. Johnson, R. K. Sheline, and R. Wolfgang, Phys. Rev. **102**, 831 (1956).
[40] V. Fedoseyev *et al.*, Hyperfine Interact. **127**, 409 (2000).
[41] A. Jokinen *et al.*, Nucl. Instrum. Methods Phys. Res., Sect. B **126**, 95 (1997).
[42] F. Ames, G. Bollen, P. Delahaye, F. O., G. Huber, O. Kester, K. Reisinger, and P. Schmidt, Nucl. Instrum. Methods Phys. Res., Sect. A **538**, 17 (2005).
[43] R. Rao, O. Kester, T. Sieber, D. Habs, and K. Rudolph, Nucl. Instrum. Methods Phys. Res., Sect. A **427**, 170 (1999).

[44] T. Sieber, O. Kester, D. Habs, S. Emhofer, K. Rudolph, H. Bongers, A. Schempp, and U. Ratzinger, Nucl. Phys. A **701**, 656 (2002).
[45] V. Bildstein *et al.*, Eur. Phys. J. A **48**, 85 (2012).
[46] N. Warr *et al.*, Euro. Phys. J. A **49**, 40 (2013).
[47] J. Eberth *et al.*, in *AIP Conference Proceedings*, Vol. 656, American Institute of Physics Conference Series (AIP, College Park, 2003), pp. 349–356.
[48] E. J. Sternglass, Phys. Rev. **108**, 1 (1957).
[49] D. J. Millener, D. E. Alburger, E. K. Warburton, and D. H. Wilkinson, Phys. Rev. C **26**, 1167 (1982).
[50] M. Seeger, T. Kihm, K. Knöfle, U. Schmidt-Rohr, J. Hebenstreit, D. Paul, and P. V. Rossen, Nucl. Phys. A **533**, 1 (1991).
[51] M. Seeger *et al.*, Nucl. Phys. A **539**, 223 (1992).
[52] H. Miyahara, K. Hara, C. Mori, Y. Kasugai, and K. Kawade, Nucl. Instrum. Methods Phys. Res., Sect. A **324**, 219 (1993).
[53] M. Chowdhury and H. S. Gupta, Nucl. Phys. A **205**, 454 (1973).
[54] R. Fulmer *et al.*, Phys. Rev. **133**, B955 (1964).
[55] E. Wesolowski *et al.*, J. Phys. G: Nucl. Part. Phys. **17**, 955 (1991).
[56] E. Cosman *et al.*, Phys. Rev. **163**, 1134 (1967).
[57] R. H. Fulmer and A. L. McCarthy, Phys. Rev. **131**, 2133 (1963).
[58] T. Anfinsen *et al.*, Nucl. Phys. A **157**, 561 (1970).
[59] G. Huttlin *et al.*, Nucl. Phys. A **227**, 389 (1974).
[60] I. Turkiewicz *et al.*, Nucl. Phys. A **143**, 641 (1970).
[61] S. Agostinelli *et al.*, Nucl. Instrum. Methods Phys. Res., Sect. A **506**, 250 (2003).
[62] I. J. Thompson, Comput. Phys. Rep. **7**, 167 (1988).
[63] J. Lohr and W. Haeberli, Nucl. Phys. A **232**, 381 (1974).
[64] H. An and C. Cai, Phys. Rev. C **73**, 054605 (2006).
[65] Y. Han, Y. Shi, and Q. Shen, Phys. Rev. C **74**, 044615 (2006).
[66] A. Koning and J. Delaroche, Nucl. Phys. A **713**, 231 (2003).
[67] F. G. Perey, Phys. Rev. **131**, 745 (1963).
[68] B. Morillon and P. Romain, Phys. Rev. C **76**, 044601 (2007).
[69] X. Li and C. Cai, Nucl. Phys. A **801**, 43 (2008).
[70] N. B. Nguyen, F. M. Nunes, and R. C. Johnson, Phys. Rev. C **82**, 014611 (2010).
[71] N. K. Timofeyuk and R. C. Johnson, Phys. Rev. Lett. **110**, 112501 (2013).
[72] A. M. Mukhamedzhanov and F. M. Nunes, Phys. Rev. C **72**, 017602 (2005).
[73] E. Runte *et al.*, Nucl. Phys. A **441**, 237 (1985).
[74] P. Endt, At. Data Nucl. Data Tables **23**, 3 (1979).
[75] A. Harder, S. Michaelsen, K. Lieb, and A. Williams, Z. Phys. A **345**, 143 (1993).
[76] G. Vourvopoulos *et al.*, Nucl. Phys. A **174**, 581 (1971).
[77] L. R. Medsker, H. T. Fortune, S. C. Headley, and J. N. Bishop, Phys. Rev. C **12**, 1516 (1975).
[78] K. Knöpfle, M. Rogge, C. Mayer-Boricke, J. Pedersen, and D. Burch, Nucl. Phys. A **159**, 642 (1970).
[79] J. P. Schiffer *et al.*, Phys. Rev. Lett. **108**, 022501 (2012).
[80] J. P. Schiffer *et al.*, Phys. Rev. C **87**, 034306 (2013).
[81] M. H. Macfarlane and J. B. French, Rev. Mod. Phys. **32**, 567 (1960).
[82] F. Recchia *et al.*, Phys. Rev. C **85**, 064305 (2012).
[83] P. Li, W. Daehnick, S. K. Saha, J. Brown, and R. Kouzes, Nucl. Phys. A **469**, 393 (1987).
[84] X. Ji and B. H. Wildenthal, Phys. Rev. C **40**, 389 (1989).